

Supplementary Materials for

Artificial intelligence-enabled caregiving walking stick powered by ultra-low frequency human motion

Xinge Guo, Tianyiyi He, Zixuan Zhang, Anxin Luo, Fei Wang*, Eldwin J. Ng, Yao Zhu, Huicong Liu, and Chengkuo Lee*

*Corresponding author. Email: elelc@nus.edu.sg (C. Lee); wangf@sustech.edu.cn (F. Wang)

This PDF file includes:

Note S1. Designs and working principles of the hybridized unit.

Note S2. Optimization strategy for the P-TENG.

Note S3. Fabrication methods for each part.

Note S4. Strike speed sensing by R-TENG.

Note S5. Equations for calculating four parameters used for assessing the correlation between two parameters.

Figure S1. Photos and schematics of the proposed hybridized unit with linear-to-rotary structure, its main functional parts, and correspond working principles.

Figure S2. Photo of the 3D-printed mold for fabricating the Ecoflex layer with small frustums on it.

Figure S3. Photos of the pawl-ratchet system.

Figure S4. Photos of the circular disk and the twist rod.

Figure S5. Output currents of three main functional units for the hybridized unit.

Figure S6. Output voltages of the rotational unit under various steps per minute.

Figure S7. Schematic of the setup for the characterization of three Ecoflex materials for the P-TENG.

Figure S8. Detailed output curves for some data points used in force sensing characterization.

Figure S9. The output of the sensing signals of the walking stick under four different floors.

Figure S10. Schematic of the setup for the strike speed sensing characterization of the R-TENG.

Figure S11. Characterization of the R-TENG for strike speed sensing.

Figure S12. The output of the walking stick under the circumstances that may be confused with falling down, including dropping down, picking up, and putting down the walking stick.

Figure S13. Sensing output of the environmental temperature and humidity sensing module applied in the self-sustained IoT system.

Table S1. Comparison of the output performance between previously proposed wearable energy harvesters (EHs) and the proposed rotational unit in this work.

Video S1. Demonstration of the in-door healthcare monitoring with the caregiving walking stick.

Video S2. Demonstration of the omni-monitoring with the caregiving walking stick.

References (1 to 25)

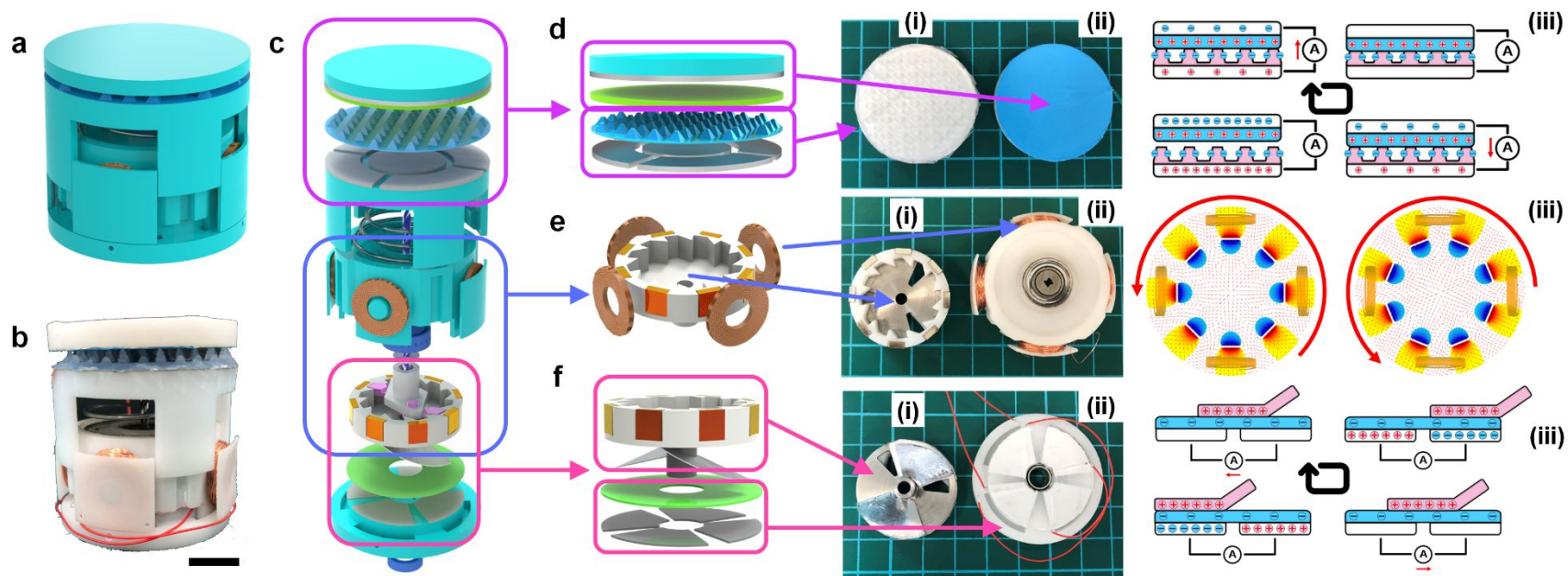


Figure S1. Photos and schematics of the proposed hybridized unit with linear-to-rotary structure, its main functional parts, and corresponding working principles. (a) Schematic of the proposed hybridized unit. (b) Photo of the proposed hybridized unit. (c) Exploded view of the hybridized unit. (d) P-TENG: (i) the Ecoflex layer with small frustum structures on the surface attached to an aluminum layer, (ii) the nitrile layer attached on the surface of an aluminum layer, (iii) working principle. (e) EMG: (i) Eight magnets are evenly distributed on the outside of the ratchet, (ii) four copper coils with 500 turns for each coil are mounted outside the casing, (iii) working principle. (f) R-TENG: (i) Two symmetrical aluminum fans are attached at the bottom surface of the ratchet, (ii) The bottom aluminum electrodes are cut to four separate parts with two of them facing in the opposite side linked together through a wire, (iii) working principle.

Note S1. Designs and working principles of the hybridized unit. As shown in Figure S1c, the mainframe of the hybridized unit contains the top cap, the lid, the casing, and the bottom pedestal, which were fabricated through a low-cost 3D printing process made by a UV resin material, with the photo shown in Figure S1b. And for the other core components, which are also the parts that suffering the largest pressure and friction, materials with high tensile and abrasiveness to avoid wearing out and increase the cycle life were chosen. The circular disk is made of high-speed steel with quenching. The twist rod is made of stainless steel. And the pawl is made of aluminum alloy. The hybridized unit contains three main functional components, as depicted in Figure S1d-f, which are the P-TENG, EMG, and R-TENG, respectively, with their relative locations corresponding to Figure S1c. For the P-TENG located at the top of the device, the Ecoflex and Nitrile materials were applied as the negative and positive triboelectrification layers, and two aluminum electrode layers were attached to them to conduct the transferred charges. Small frustrum structures at the front side of the Ecoflex layer were fabricated through a 3D printed mold (Figure S2) to increase the sensing range and the sensitivity. For the P-TENG works in the contact-separation mode, the top nitrile layer carrying static positive charges and the bottom Ecoflex layer carrying static negative charges will lead to charges transferred between two aluminum electrodes in the process of contact-separation due to electrostatic induction, thus generate the triboelectric output (Figure S1d(iii)). Located at the middle part of the device is the EMG aiming at harvesting the biomechanical energy, containing four sets of coils wrapped outside the casing and eight magnets (Nd-Fe-B-N52) evenly distributed on the ratchet (Figure S1e). These four coils are connected in series with each other to improve the output voltage. Figure S1e(iii) shows the distribution of magnetic lines of flux simulated through Finite Element Analysis. Eight magnets are fixed on the rotating ratchet and cause the continuous variation of magnetic flux passing through the four coils mounted on the casing, thus further generate the induced current. The bottom R-TENG contains two aluminum fans fixed on the backside of the ratchet designed to reduce the rotation friction without compromising the contact area, and a Polytetrafluoroethylene (PTFE) film adhered to an aluminum layer attached on the front side of the pedestal (see Figure S1f). With the ratchet's rotation, two aluminum fans attached to the bottom of it will keep sliding on the bottom PTFE layer. The difference of the overlapping layer with an aluminum fan between two electrodes will lead to the transferring of charges and continuously generate current, as depicted in Figure S1f(iii)

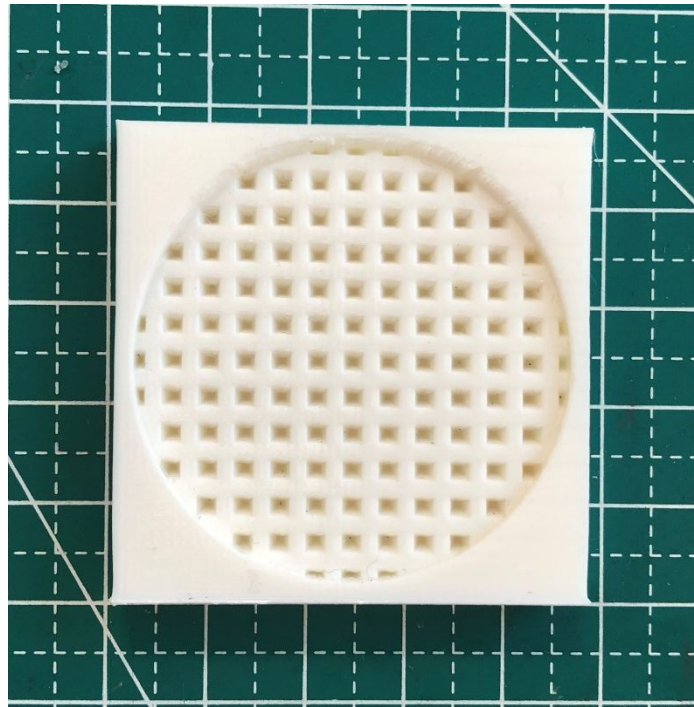


Figure S2. Photo of the 3D-printed mold for fabricating the Ecoflex layer with small frustums on it.

Note S2. Optimization strategy for the P-TENG. The mm-scale frustum structure was designed to be patterned on the Ecoflex surface. Compared to the Ecoflex layer without surface modification, these frustum structures help the Ecoflex to increase its sensitivity and sensing range. At the same time, the output voltage is also improved for enlarged contact areas and spacing.

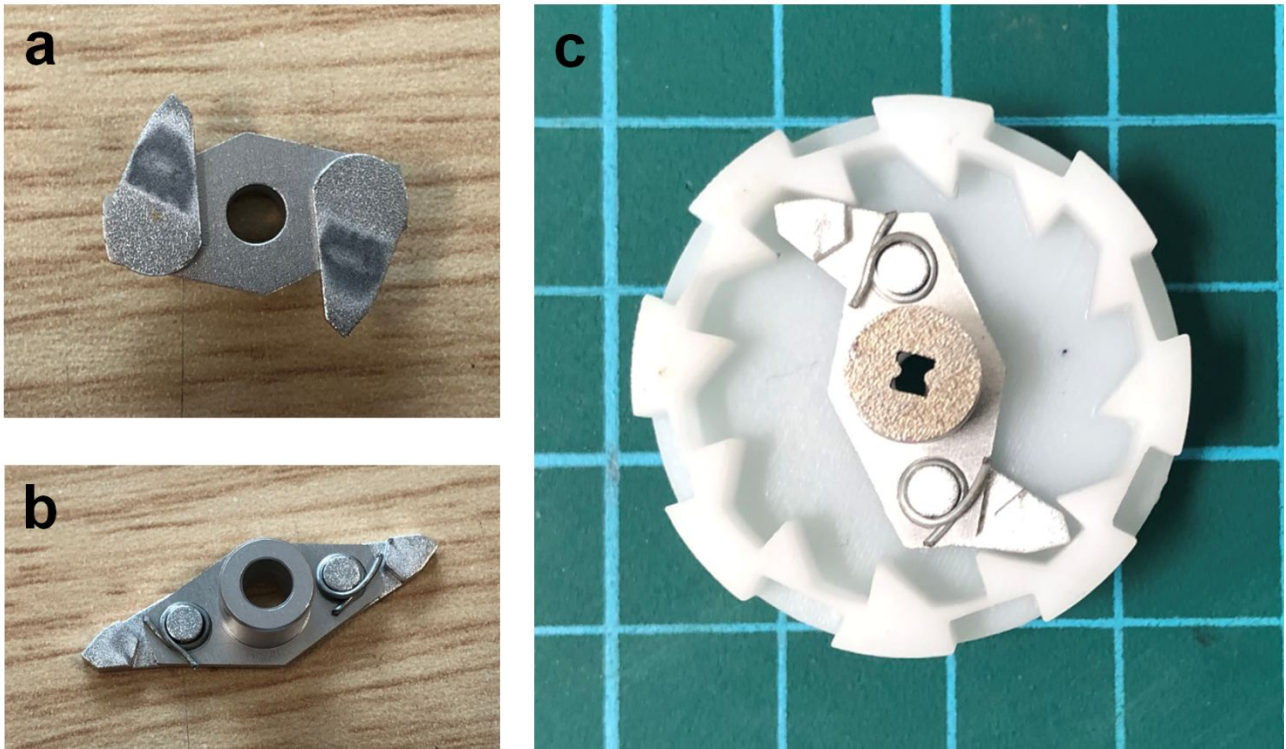


Figure S3. Photos of the pawl-ratchet system. Photos of the pawl and two claws were taken from (a) backside and (b) front side. The two claws are fixed on the pawl through two bent iron wires. (c) Photo of the pawl-ratchet system placed on a cutting mat with one square standing for an area of $1\text{ cm} \times 1\text{ cm}$. The circular disk is also placed on the top of the pawl, which can be solidly fixed to the pawl through the inner wall of the top bearing. This photo shows the driving status, in which the two claws are spreading out due to rotating and embed to the ratchet's inner indentation.

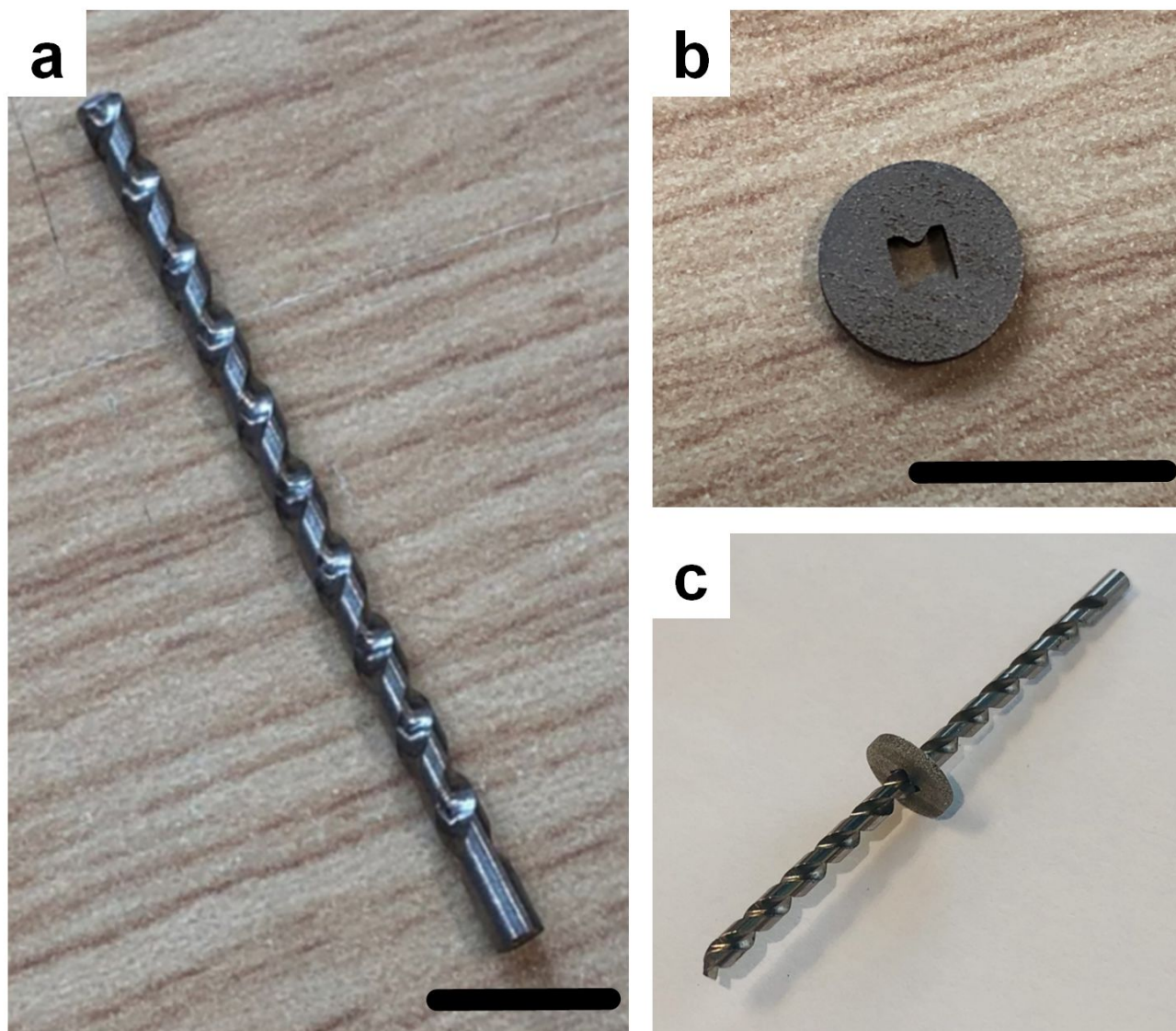


Figure S4. Photos of the circular disk and the twist rod. (a) Photo of the twist rod. The bottom side without the pattern is used to be fixed in the top lid, while the twist rod is plugged into the circular disk through the top side. (b) The photo of the circular disk. The dumbbell-shaped hole is designed to match with the patterns on the twist rod, through which the linear motion of the twist rod can drive the circular disk to rotate. (c) The photo shows the collaboration between the twist rod and the circular disk.

Note S3. Fabrication for each part. The outer frame of the proposed device, including the top cap, lid, casing, and pedestal, are all fabricated through low-cost 3D printing. Other parts that will endure large force are fabricated through casting by stainless steel, including the twist rod, the pawl, claws, and the circular disk. Besides, the ratchet is also fabricated with stainless steel to increase its mass to increase the rotation inertia, which will help to improve the rotation time.

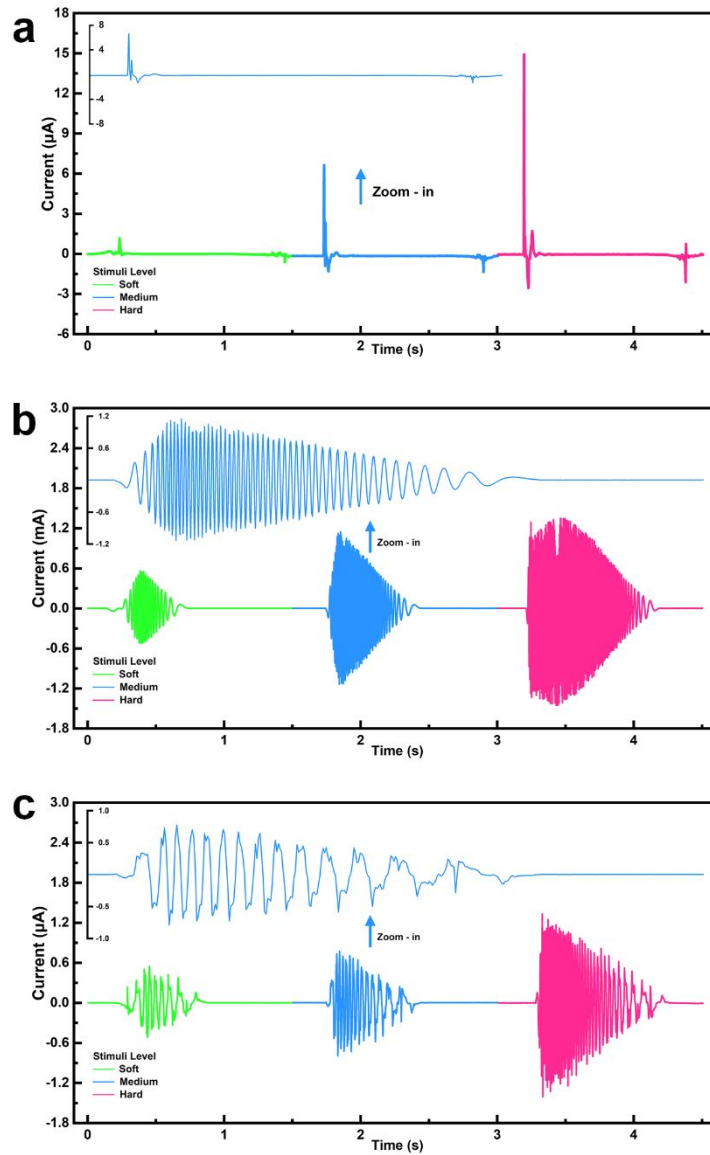


Figure S5. Output currents of three main functional units for the hybridized unit. (a) The output current for the top P-TENG under three different level stimuli, with the zoom-in figure of the output curve under the medium stimulus. (b) The output current for the middle EMG under three different level stimuli, with the zoom-in figure of the output curve under the medium stimulus. (c) The output current for the bottom R-TENG under three different level stimuli, with the zoom-in figure of the output curve under the medium stimulus.

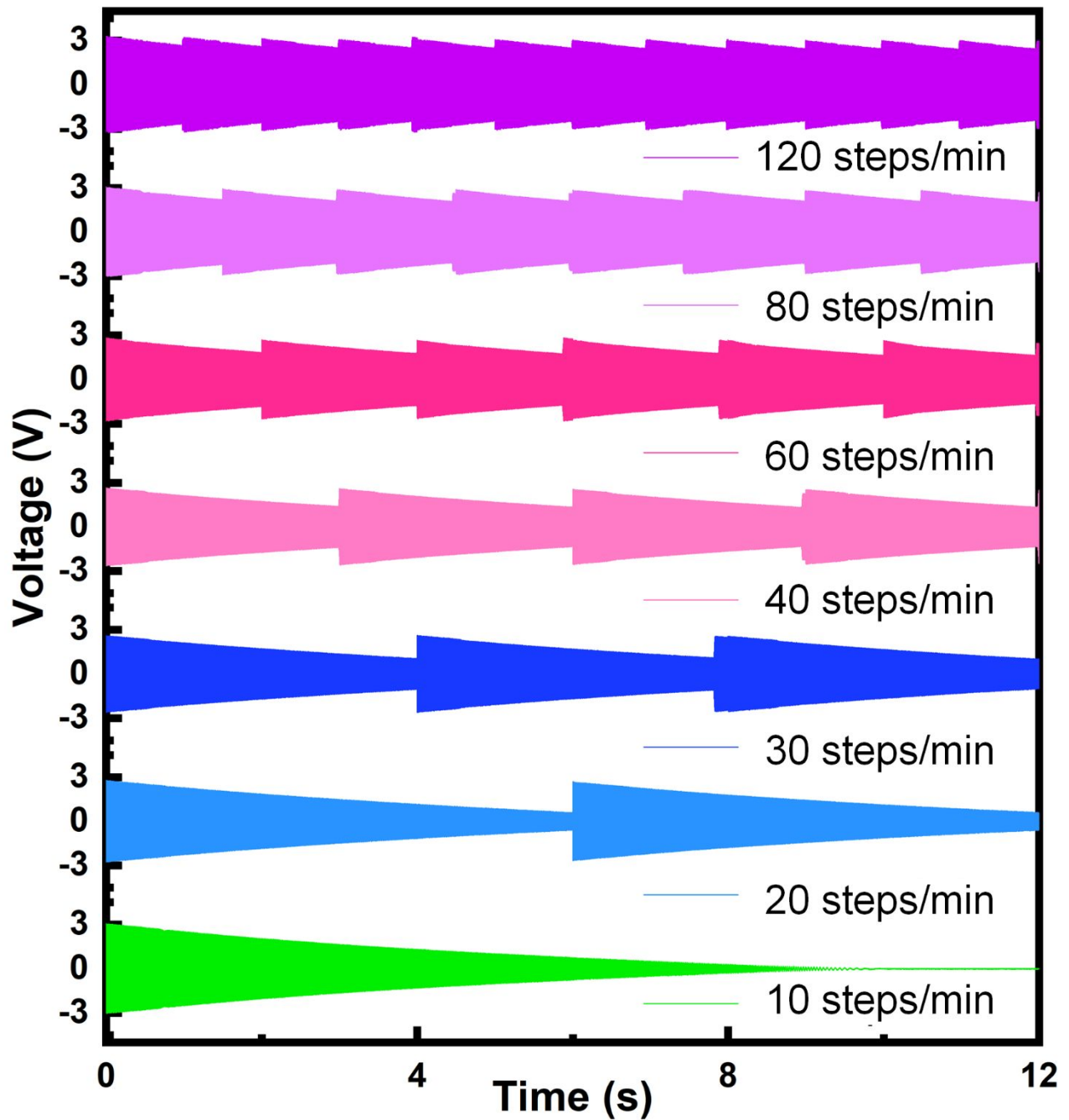


Figure S6. Output voltages of the rotational unit under various steps per minute. This figure shows a time interval of 12 s. We can notice that due to the ratchet can still keep rotating based on its rotation inertia for a maximum time around 10 s, a decrease of the step frequency doesn't have a significant influence on the output.

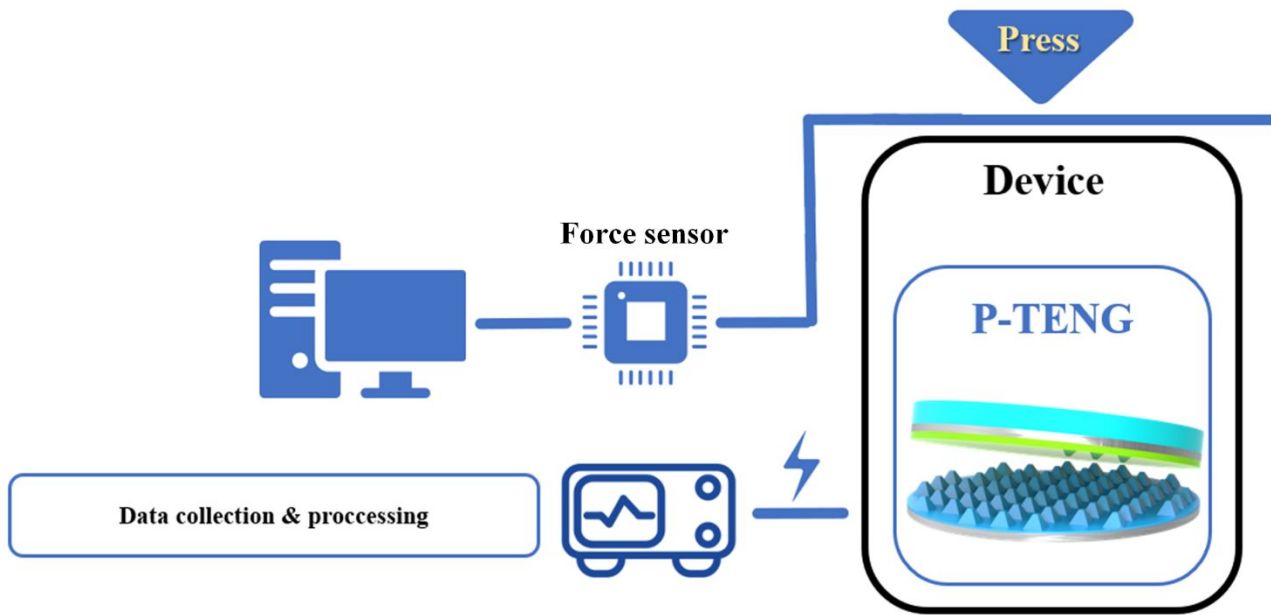


Figure S7. Schematic of the setup for the characterization of three Ecoflex materials for the P-TENG. The applied force is sensed by a force sensor through a force gauge linked to a computer. Compared to the proposed P-TENG with five separate electrodes, this measurement uses one whole electrode instead (area size: 13.2 cm²). The open-circuit output voltage of the P-TENG is collected by an oscilloscope (Agilent, InfiniiVision, DSO-X 3034A) and an Electrometer (Keithley 6514) with the normal probe 10 M Ω .

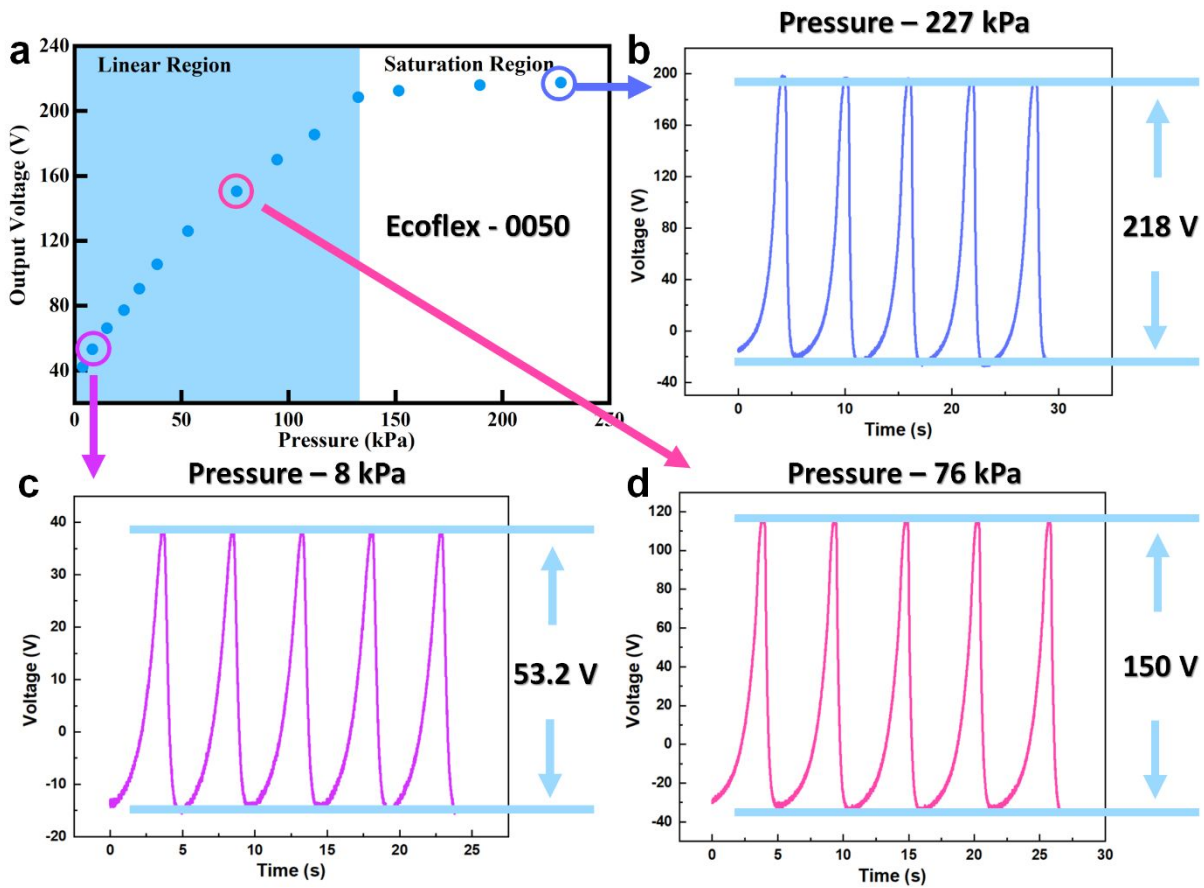


Figure S8. Detailed output curves for some data points used in force sensing characterization. (a) The open-circuit output voltage for the P-TENG with a single electrode under different applied pressures. (b) The output curve under 227 kPa applied pressure, with an average open-circuit voltage of 218 V. (c) The output curve under 8 kPa applied pressure, with an average open-circuit voltage of 53.2 V. (d) The output curve under 76 kPa applied pressure applied force, with an average open-circuit voltage of 150 V.

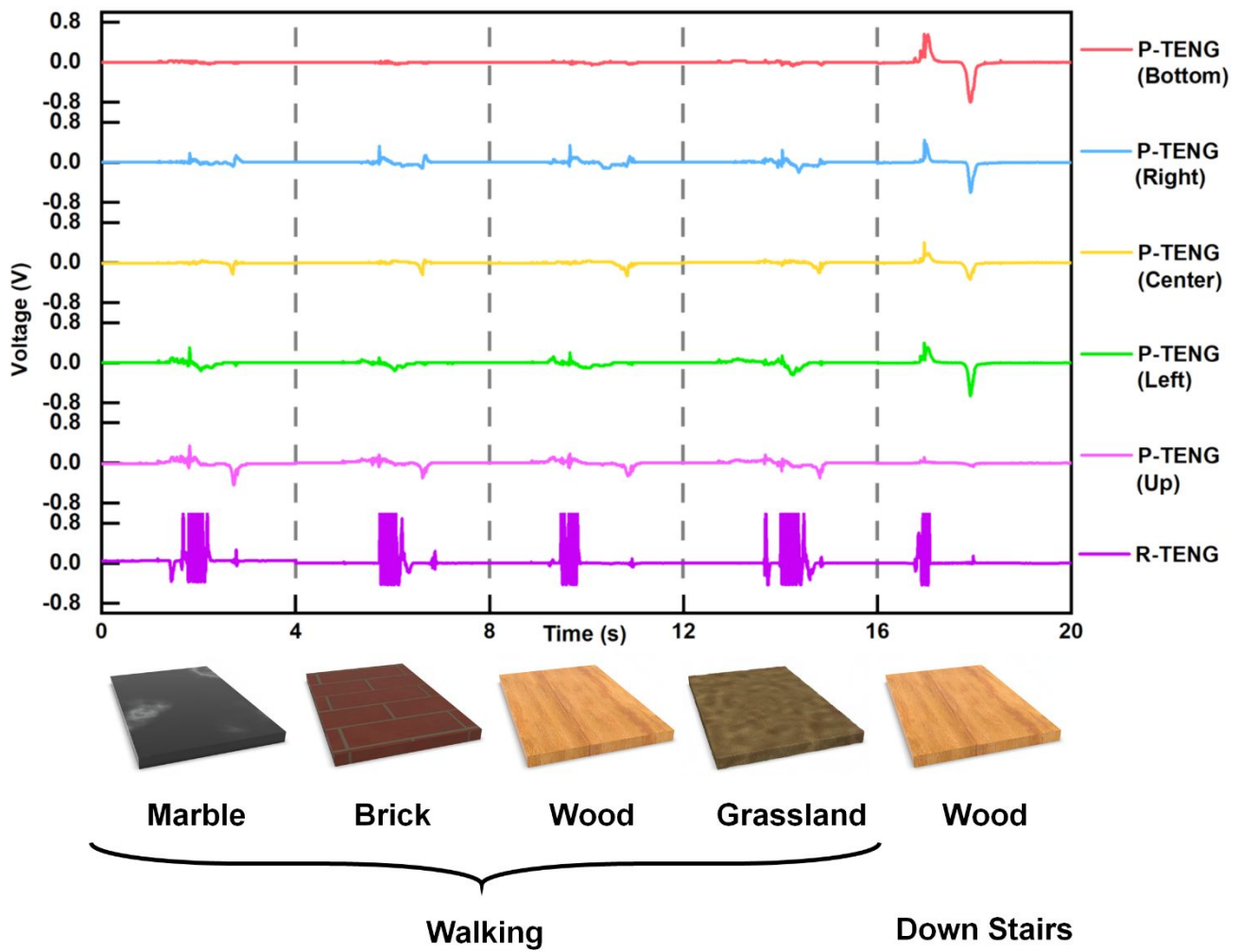


Figure S9. The output of the sensing signals of the walking stick under four different floors. The tiny variance of the signal may mainly come from the inconsistency of the walking, and it can be noticed that this variance is very inapparent compared to the difference between movements.

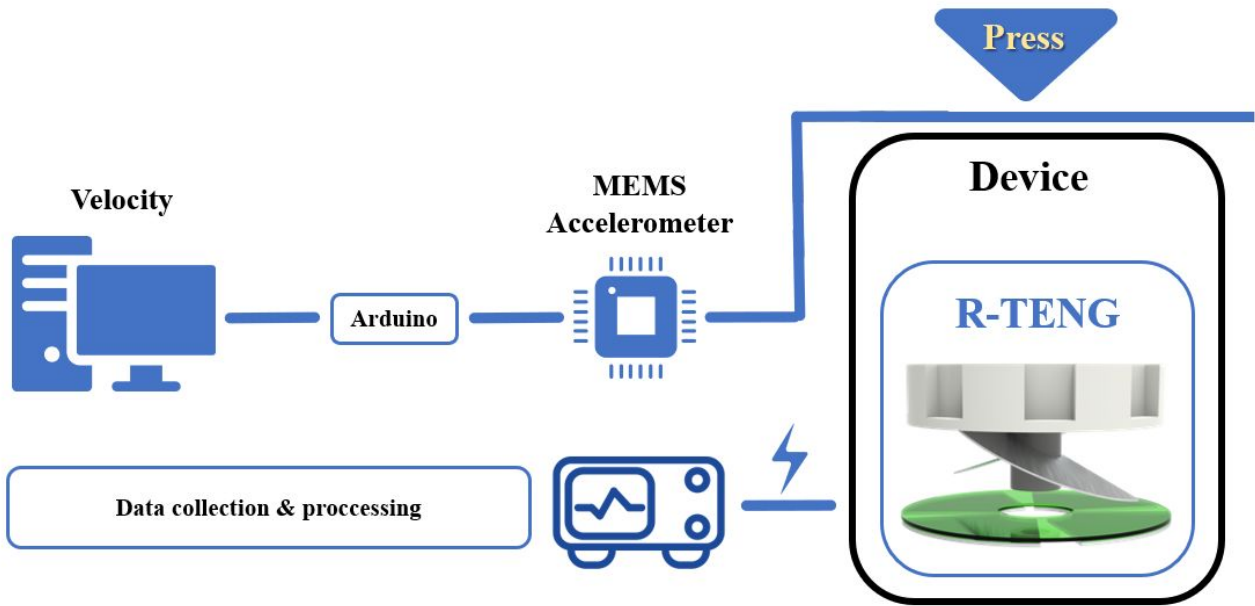


Figure S10. Schematic of the setup for the strike speed sensing characterization of the R-TENG. The MEMS accelerometer is mounted on the top lid of the device to detect the real-time acceleration of the motion. The signals of the MEMS accelerometer are collected by an Arduino MEGA 2560 microcontroller then sent to the computer through a USB cable for data analysis. Simultaneously, the output of the R-TENG is collected by an oscilloscope (Agilent, InfiniiVision, DSO-X 3034A) with a 100M Ω probe.

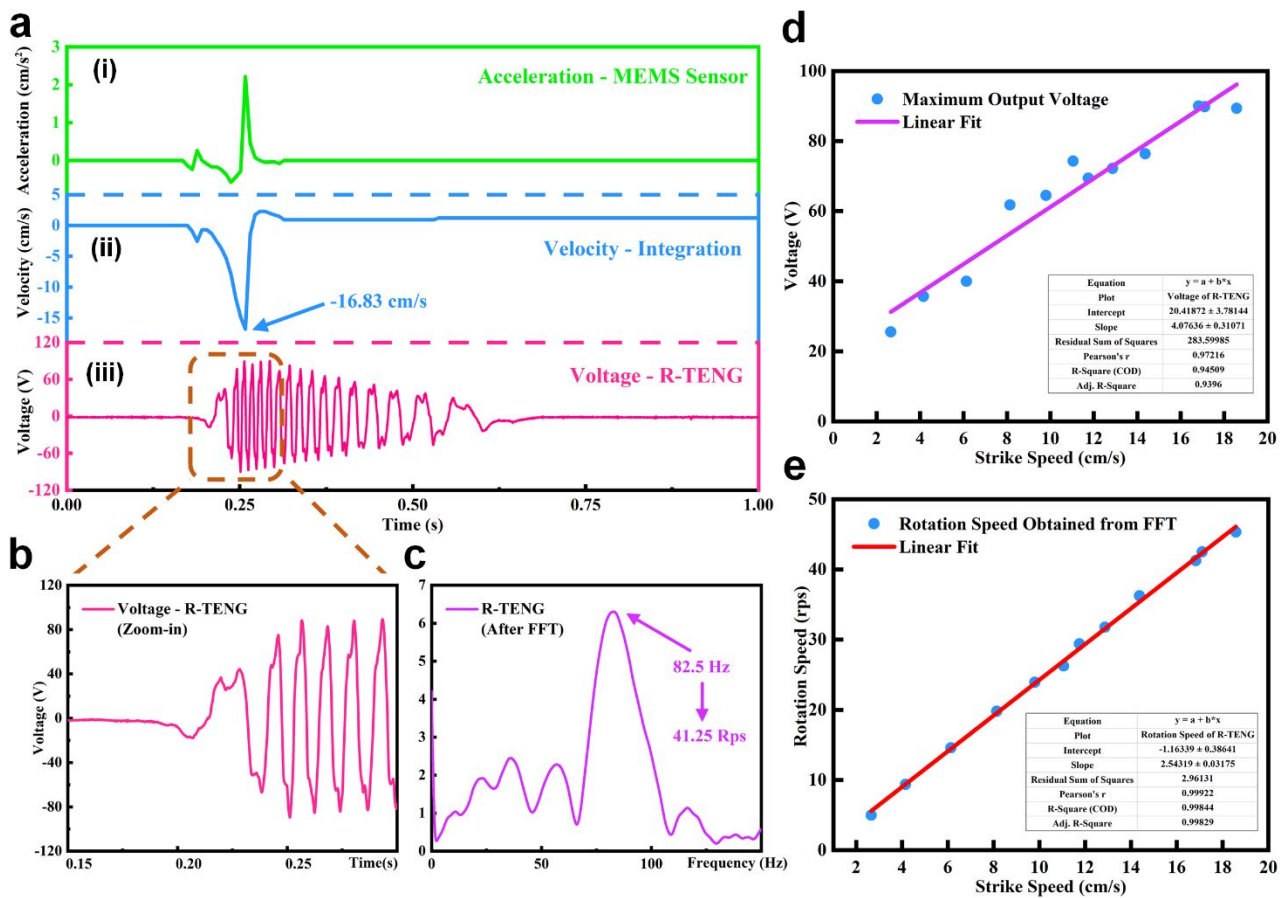


Figure S11. Characterization of the R-TENG for strike speed sensing. (a) Signals collected from MEMS accelerometer and the R-TENG under single external stimulus: (i) real-time acceleration of the external stimuli, (ii) the velocity obtained from the integration of the measured acceleration with time, (iii) corresponding output voltage of the R-TENG under this stimulus. (b) Zoom-in of the output curve of R-TENG in the time interval between applying and releasing the external stimulus. (c) FFT results for the output curve shown in Figure S11b to obtain the rotation speed. (d) The maximum output voltage under various strike speeds and the linear fitting curve with parameters for assessment. (e) The rotation speed obtained from FFT under various strike speeds and the linear fitting curve with parameters for assessment.

Note S4. Strike speed sensing by R-TENG. In the proposed hybridized unit, R-TENG is utilized to measure the strike speed for each time the walking stick contact with the ground and monitor if the user is in normal motion status. For the R-TENG part, the bottom electrode has been cut into four fan-shaped structures, and each two in the opposite direction are connected to form a single output. Simultaneously, a commercial MEMS accelerometer was applied to measure the actual acceleration of the external stimuli and further obtain the maximum strike speed by integrating the acceleration with time, with the detailed setup shown in Figure S9. The output for the MEMS sensor and the R-TENG under one stimulus is shown in Figure S11a. In one striking, the device will first undergo a downward acceleration with an increasing downward speed. When the lid reaches the bottom, it will stop moving instantaneously through a collide with a large upward acceleration. In this process, the ratchet will reach the maximum rotation speed as the velocity reaches the maximum value due to the mechanical linkage of the linear-to-rotary structure discussed before. And it will keep rotating for a while till stopped by the friction. Generally, the method used to sense the maximum velocity is to characterize its linear relationship with the maximum output voltage of the R-TENG as the linear fitting curve shown in Figure S11d. At the same time, several critical parameters to measure the linear correlation between two data sets, including the Residual Sum of Squares (RSS), Pearson's r (Pearson correlation coefficient, PCC), R-square (Coefficient of determination, R^2), and Adj. R^2 (Adjusted R-Square), are listed inside the figure, and their calculation methods are discussed in Note S5. Although the value of R^2 and PCC is close to 1, in which we can tell that the maximum output voltage of R-TENG does have a linear correlation with the strike speed to a certain extent, the considerable value of RSS and the value of adjusted R^2 also imply that there exist other potential variables influencing the voltage in addition to the strike speed. This is consistent with the features of TENG's output, which can be affected by the environment temperature, environment humidity, and also the contact area. Considering the practical applications of walking sticks, which need to be used in various environments, sensing barely relied on the output voltage may cause instability. Thanks to the mechanical relationship between the rotation of the R-TENG and the linear motion of the applied stimuli, we can also obtain the strike speed through the rotation speed of the R-TENG. After doing the Fast Fourier Transform (FFT) for the curve shown in Figure S11b, it can be noticed that the maximum signal appears at the frequency of 82.5 Hz, which stands for the actual rotation speed of 41.25 revolutions per second (rps). This is because two aluminum fans will double the frequency of the generated voltage. Since the mechanical linkage is more stable and reliable with minimal influences from environmental aspects, a better linear fitting curve can be obtained between the rotation speed and the strike speed, as shown in Figure S11e. Compared to the parameters in Figure S11d, a much smaller RSS value is obtained, while the values of PCC, R^2 , and Adj. R^2 , are also closer to 1. This means that the strike speed can almost be perfectly explained by the rotation speed, and there are barely any other potential variables that may also affect the rotation speed.

Figure S12.

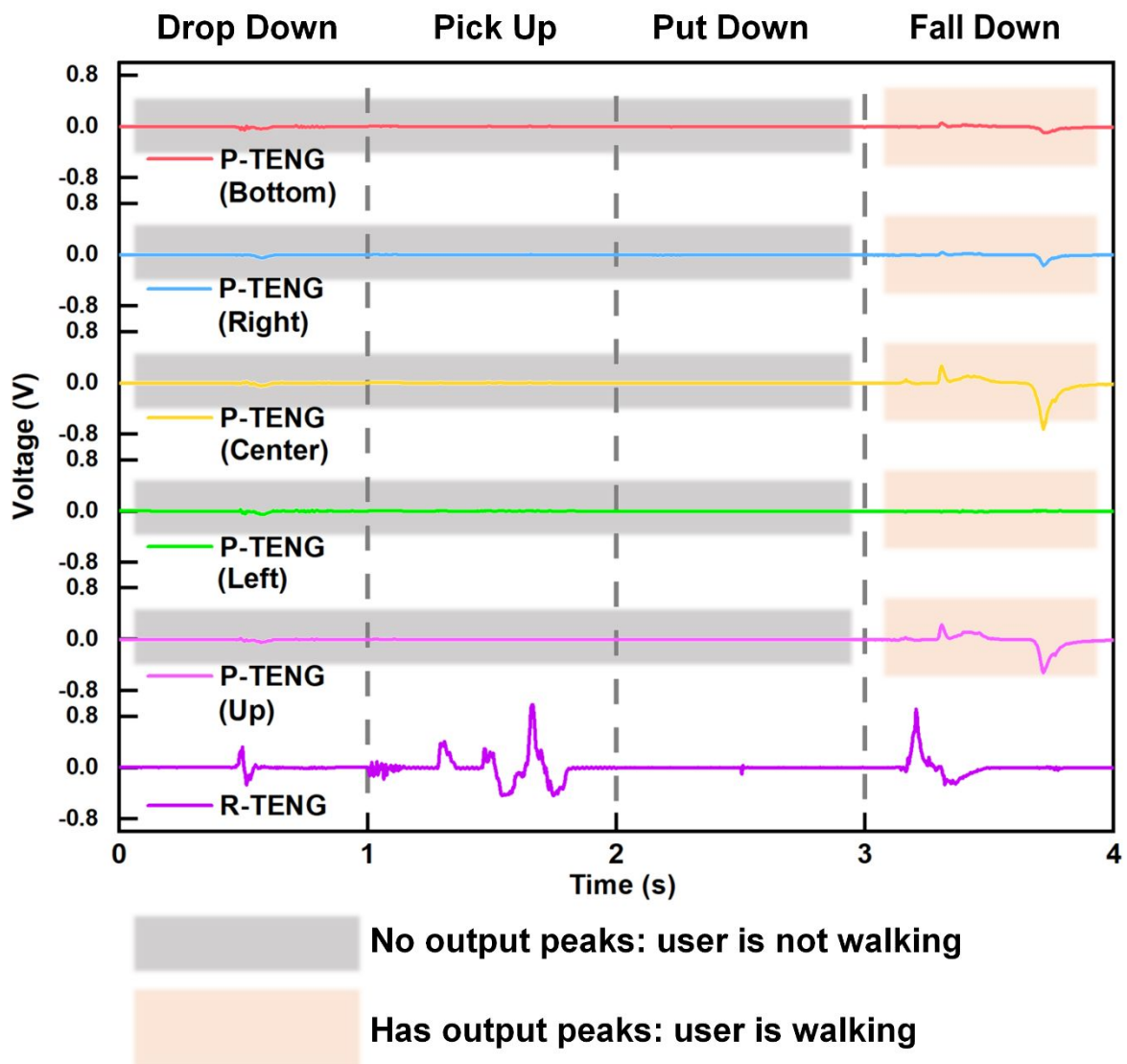


Figure S12. The output of the walking stick under the circumstances that may be confused with falling down, including dropping down, picking up, and putting down the walking stick. It can be noticed that although they have similar output from the R-TENG to the falling down, the lack of the P-TENG can tell us the user is not actually using the walking stick.

Figure S13.

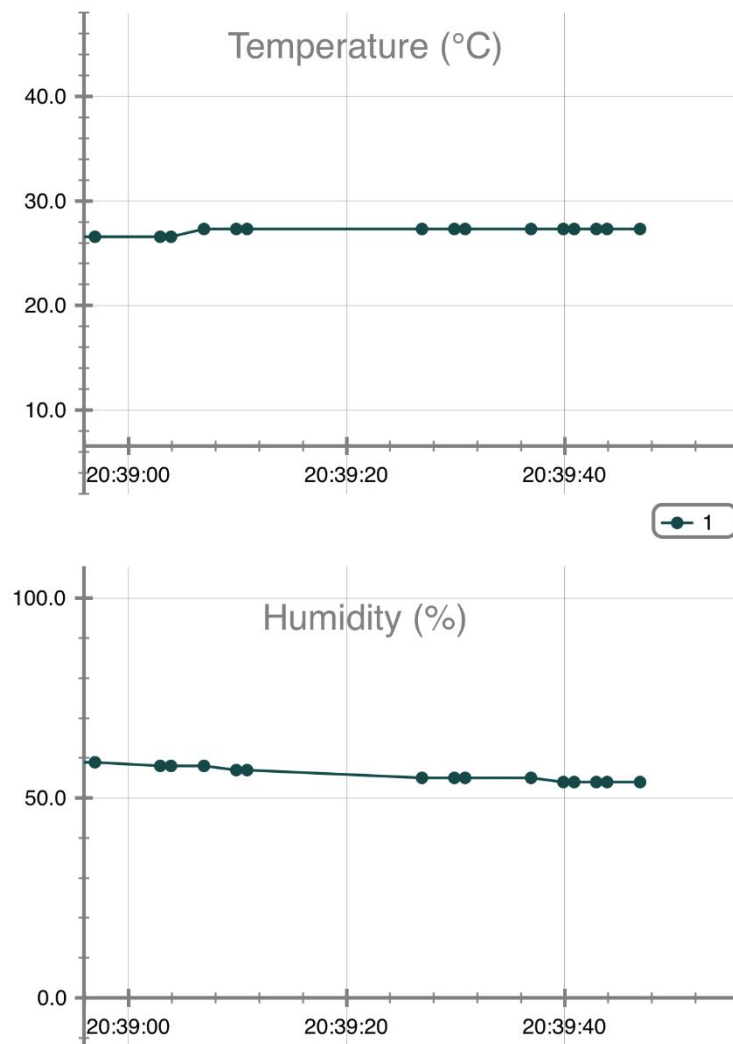


Figure S12. Sensing output of the environmental temperature and humidity sensing module applied in the self-sustained IoT system. The sensing data is obtained from a commercial IoT module CYALKIT-E02 which is able to sense the real-time environmental temperature and humidity data and send it wirelessly through an embedded Bluetooth module. We removed the solar cell used in this IoT module and powered it continuously through the 2 F supercapacitor, which stored the energy generated from two power units.

Note S5. Equations for calculating four parameters used for assessing the correlation between two parameters.

Residual sum of squares (RSS):

$$RSS = \sum_{i=1}^n (y_i - f(x_i))^2$$

Pearson correlation coefficient (Pearson's r, PCC):

$$r = \frac{\sum (x_i - \bar{x})(y_i - \bar{y})}{\sqrt{\sum (x_i - \bar{x})^2 \sum (y_i - \bar{y})^2}}$$

Coefficient of determination (R-square, R²):

$$R^2 = 1 - \frac{RSS}{TSS} = 1 - \frac{\sum_{i=1}^n (y_i - f(x_i))^2}{\sum_{i=1}^n (y_i - \bar{y})^2}$$

Adjusted R-square (adj. R²):

$$adj. R^2 = 1 - \frac{(1 - R^2)(n - 1)}{n - p - 1}$$

x_i and y_i means the corresponding values of x and y from the measurements, while $f(x_i)$ means the value from the fitting curve when x equals to x_i . \bar{x} and \bar{y} stand for the mean values of x-variable and y-variable in the sample, calculated by:

$$\bar{x} = \frac{1}{n} \sum x_i$$

$$\bar{y} = \frac{1}{n} \sum y_i$$

P stands for the total number of explanatory variables in the model, which value is 1 for the analysis in this manuscript. **n** is the sample size, which value is 12 for the analysis in this manuscript.

Table S1. Comparison of the output performance between previously proposed wearable energy harvesters (EHs) and the proposed rotational unit in this work^[1–25]. For flexible designs, their volumes are calculated through the thickness proposed in the corresponding paper. The value listed in the row of ‘Frequency’ means the frequency the device reaching its maximum power. The peak power stands for the value calculated through instantaneous peak voltage under matching resistance. And the average power is calculated through the energy generated in a certain time divided by the time interval. The values of peak power and average power are all provided by corresponding papers.

Type	Structure	Volume (cm ³)	Area (cm ²)	Frequency	Operational Bandwidth	Peak Power (mW)	Average Power (mW)	Peak Power Density	Average Power Density
PENG & TENG ¹	Non-flexible	\	\	Hand shaking	\	0.581	\	\	\
EMG & TENG ²	Non-flexible	38.88	\	22.5 Hz	\	8	\	0.206 mW cm ⁻³	\
PEG & EMG ³	Non-flexible	8.462	\	6 Hz	2 ~ 12 Hz	1.42	\	0.164 mW cm ⁻³	\
PEG ⁴	Non-flexible	0.264	\	5 Hz	0.5 ~ 5 Hz	\	~ 0.0037	\	0.014 mW cm ⁻³
EMG & TENG ⁵	Non-flexible	~ 154	\	2 Hz	1 ~ 4 Hz	265	\	1.72 mW cm ⁻³	\
EMG & TENG ⁶	Non-flexible	~ 240	\	1 Hz	\	13.8	\	0.0575 mW cm ⁻³	\
EMG & TENG ⁷	Non-flexible	45.92	\	4.7 Hz	1 ~ 4.7 Hz	131.4	\	2.86 mW cm ⁻³	\
PENG & EMG & TENG ⁸	Non-flexible	~ 11	\	5 Hz	1 ~ 5 Hz	35	\	3.2 mW cm ⁻³	\
EMG ⁹	Non-flexible	20	\	0.91 Hz	0.8 ~ 1.25 Hz	\	0.0613	\	0.0031 mW cm ⁻³
PEG ¹⁰	Non-flexible	2.8	\	34 Hz	10 ~ 34 Hz	\	0.00325	\	0.0027 mW cm ⁻³
EMG ¹¹	Non-flexible	12.7	\	8 Hz	\	\	2.46	\	0.193 mW cm ⁻³
EMG ¹²	Non-flexible	77.2	\	10 Hz	1 ~ 10 Hz	\	0.33	\	0.0043 mW cm ⁻³
EMG ¹³	Non-flexible	67.3	\	2.6 Hz	0.6 ~ 5 Hz	\	12.3	\	0.183 mW cm ⁻³
EMG & TENG ¹⁴	Non-flexible	66.11	\	5 Hz	0.25 ~ 5 Hz	~ 737.6	34.11	11.16 mW cm ⁻³	0.516 mW cm ⁻³
EMG ¹⁵	Non-flexible	11.97	\	5 Hz	0.5 ~ 5 Hz	74	8.8	6.18 mW cm ⁻³	0.735 mW cm ⁻³
EMG ¹⁶	Non-flexible	~ 29.2	\	5 Hz	\	\	3.13	\	0.107 mW cm ⁻³
TENG ¹⁷	Flexible	~ 225	~ 150	1 Hz	\	~ 718	\	0.0049 mW cm ⁻² / 0.0032 mW cm ⁻³	\
TENG ¹⁸	Flexible	\	\	3 Hz	0.5 ~ 4 Hz	\	\	0.1 mW cm ⁻²	\
TENG ¹⁹	Flexible	\	18	3 Hz	0.5 ~ 5 Hz	\	\	0.0263 mW cm ⁻²	\
TENG ²⁰	Flexible	\	\	3 Hz	1 ~ 5 Hz	\	\	0.000011 mW cm ⁻³	\
PENG ²¹	Flexible	\	\	0.6 Hz	> 0.25 Hz	\	\	0.02962 mW cm ⁻³	\
PENG ²²	Flexible	0.00006	0.12	~ 0.2 Hz	\	0.00012	\	0.001 mW cm ⁻² / 0.2 mW cm ⁻³	\
PENG ²³	Flexible	\	\	40 Hz	10 ~ 50 Hz	\	\	0.05 mW cm ⁻³	\
TENG ²⁴	Flexible	~ 18	18	3 Hz	0.5 ~ 3 Hz	\	\	\	0.00084 mW cm ⁻² / 0.00084 mW cm ⁻³
TENG ²⁵	Flexible	6.4	16	2 Hz	0.5 ~ 2.5 Hz	~ 0.1488	~ 0.00688	0.0093 mW cm ⁻² / 0.02325 mW cm ⁻³	0.00043 mW cm ⁻² / 0.001075 mW cm ⁻³
This work: EMG	Non-flexible	50	\	1 Hz	0.08 ~ 1 Hz	55	27.5	1.1 mW cm ⁻³	0.55 mW cm ⁻³

References

- (1) Chung, J.; Yong, H.; Moon, H.; Duong, Q. Van; Choi, S. T.; Kim, D.; Lee, S. Hand-Driven Gyroscopic Hybrid Nanogenerator for Recharging Portable Devices. *Adv. Sci.* **2018**, *5* (11), 1801054. <https://doi.org/10.1002/advs.201801054>.
- (2) Quan, T.; Wang, X.; Wang, Z. L.; Yang, Y. Hybridized Electromagnetic–Triboelectric Nanogenerator for a Self-Powered Electronic Watch. *ACS Nano* **2015**, *9* (12), 12301–12310. <https://doi.org/10.1021/acsnano.5b05598>.
- (3) Fan, K.; Liu, S.; Liu, H.; Zhu, Y.; Wang, W.; Zhang, D. Scavenging Energy from Ultra-Low Frequency Mechanical Excitations through a Bi-Directional Hybrid Energy Harvester. *Appl. Energy* **2018**, *216* (February), 8–20. <https://doi.org/10.1016/j.apenergy.2018.02.086>.
- (4) Li, K.; He, Q.; Wang, J.; Zhou, Z.; Li, X. Wearable Energy Harvesters Generating Electricity from Low-Frequency Human Limb Movement. *Microsystems Nanoeng.* **2018**, *4* (1), 24. <https://doi.org/10.1038/s41378-018-0024-3>.
- (5) Hou, C.; Chen, T.; Li, Y.; Huang, M.; Shi, Q.; Liu, H.; Sun, L.; Lee, C. A Rotational Pendulum Based Electromagnetic/Triboelectric Hybrid-Generator for Ultra-Low-Frequency Vibrations Aiming at Human Motion and Blue Energy Applications. *Nano Energy* **2019**, *63* (March), 103871. <https://doi.org/10.1016/j.nanoen.2019.103871>.
- (6) Jiang, D.; Ouyang, H.; Shi, B.; Zou, Y.; Tan, P.; Qu, X.; Chao, S.; Xi, Y.; Zhao, C.; Fan, Y.; Li, Z. A Wearable Noncontact Free-Rotating Hybrid Nanogenerator for Self-Powered Electronics. *InfoMat* **2020**, *2* (6), 1191–1200. <https://doi.org/10.1002/inf2.12103>.
- (7) Rahman, M. T.; Rana, S. S.; Salauddin, M.; Maharjan, P.; Bhatta, T.; Park, J. Y. Biomechanical Energy-Driven Hybridized Generator as a Universal Portable Power Source for Smart/Wearable Electronics. *Adv. Energy Mater.* **2020**, *10* (12), 1903663. <https://doi.org/10.1002/aenm.201903663>.
- (8) Tan, P.; Zheng, Q.; Zou, Y.; Shi, B.; Jiang, D.; Qu, X.; Ouyang, H.; Zhao, C.; Cao, Y.; Fan, Y.; Wang, Z. L.; Li, Z. A Battery-Like Self-Charge Universal Module for Motional Energy Harvest. *Adv. Energy Mater.* **2019**, *9* (36), 1901875. <https://doi.org/10.1002/aenm.201901875>.
- (9) Halim, M. A.; Rantz, R.; Zhang, Q.; Gu, L.; Yang, K.; Roundy, S. An Electromagnetic Rotational Energy Harvester Using Sprung Eccentric Rotor, Driven by Pseudo-Walking Motion. *Appl. Energy* **2018**, *217* (October 2017), 66–74. <https://doi.org/10.1016/j.apenergy.2018.02.093>.
- (10) Galchev, T.; Aktakka, E. E.; Najafi, K. A Piezoelectric Parametric Frequency Increased Generator for Harvesting Low-Frequency Vibrations. *J. Microelectromechanical Syst.* **2012**, *21* (6), 1311–1320. <https://doi.org/10.1109/JMEMS.2012.2205901>.
- (11) Saha, C. R.; O'Donnell, T.; Wang, N.; McCloskey, P. Electromagnetic Generator for Harvesting Energy from Human Motion. *Sensors Actuators, A Phys.* **2008**, *147* (1), 248–253. <https://doi.org/10.1016/j.sna.2008.03.008>.
- (12) Zhao, L.-C.; Zou, H.-X.; Gao, Q.-H.; Yan, G.; Liu, F.-R.; Tan, T.; Wei, K.-X.; Zhang, W.-M. Magnetically Modulated Orbit for Human Motion Energy Harvesting. *Appl. Phys. Lett.* **2019**, *115* (26), 263902. <https://doi.org/10.1063/1.5131193>.
- (13) Fan, K.; Cai, M.; Wang, F.; Tang, L.; Liang, J.; Wu, Y.; Qu, H.; Tan, Q. A String-Suspended and Driven Rotor for Efficient Ultra-Low Frequency Mechanical Energy Harvesting. *Energy Convers. Manag.* **2019**, *198* (July), 111820. <https://doi.org/10.1016/j.enconman.2019.111820>.
- (14) Maharjan, P.; Bhatta, T.; Cho, H.; Hui, X.; Park, C.; Yoon, S.; Salauddin, M.; Rahman, M. T.; Rana, S. S.; Park, J. Y. A Fully Functional Universal Self-Chargeable Power Module for Portable/Wearable Electronics and Self-Powered IoT Applications. *Adv. Energy Mater.* **2020**, *10* (48), 2002782. <https://doi.org/10.1002/aenm.202002782>.

- (15) Maharjan, P.; Bhatta, T.; Salauddin Rasel, M.; Salauddin, M.; Toyabur Rahman, M.; Park, J. Y. High-Performance Cycloid Inspired Wearable Electromagnetic Energy Harvester for Scavenging Human Motion Energy. *Appl. Energy* **2019**, *256* (July), 113987. <https://doi.org/10.1016/j.apenergy.2019.113987>.
- (16) Wu, Z.; Tang, J.; Zhang, X.; Yu, Z. An Energy Harvesting Bracelet. *Appl. Phys. Lett.* **2017**, *111* (1), 013903. <https://doi.org/10.1063/1.4991666>.
- (17) Zhou, Z.; Weng, L.; Tat, T.; Libanori, A.; Lin, Z.; Ge, L.; Yang, J.; Chen, J. Smart Insole for Robust Wearable Biomechanical Energy Harvesting in Harsh Environments. *ACS Nano* **2020**, *14* (10), 14126–14133. <https://doi.org/10.1021/acsnano.0c06949>.
- (18) Li, S.; Wang, J.; Peng, W.; Lin, L.; Zi, Y.; Wang, S.; Zhang, G.; Wang, Z. L. Sustainable Energy Source for Wearable Electronics Based on Multilayer Elastomeric Triboelectric Nanogenerators. *Adv. Energy Mater.* **2017**, *7* (13), 1602832. <https://doi.org/10.1002/aenm.201602832>.
- (19) Dong, K.; Deng, J.; Zi, Y.; Wang, Y.-C.; Xu, C.; Zou, H.; Ding, W.; Dai, Y.; Gu, B.; Sun, B.; Wang, Z. L. 3D Orthogonal Woven Triboelectric Nanogenerator for Effective Biomechanical Energy Harvesting and as Self-Powered Active Motion Sensors. *Adv. Mater.* **2017**, *29* (38), 1702648. <https://doi.org/10.1002/adma.201702648>.
- (20) Dong, K.; Deng, J.; Ding, W.; Wang, A. C.; Wang, P.; Cheng, C.; Wang, Y.-C.; Jin, L.; Gu, B.; Sun, B.; Wang, Z. L. Versatile Core-Sheath Yarn for Sustainable Biomechanical Energy Harvesting and Real-Time Human-Interactive Sensing. *Adv. Energy Mater.* **2018**, *8* (23), 1801114. <https://doi.org/10.1002/aenm.201801114>.
- (21) Mokhtari, F.; Foroughi, J.; Zheng, T.; Cheng, Z.; Spinks, G. M. Triaxial Braided Piezo Fiber Energy Harvesters for Self-Powered Wearable Technologies. *J. Mater. Chem. A* **2019**, *7* (14), 8245–8257. <https://doi.org/10.1039/c8ta10964h>.
- (22) Wu, W.; Bai, S.; Yuan, M.; Qin, Y.; Wang, Z. L.; Jing, T. Lead Zirconate Titanate Nanowire Textile Nanogenerator for Wearable Energy-Harvesting and Self-Powered Devices. *ACS Nano* **2012**, *6* (7), 6231–6235. <https://doi.org/10.1021/nn3016585>.
- (23) Sim, H. J.; Choi, C.; Lee, C. J.; Kim, Y. T.; Spinks, G. M.; Lima, M. D.; Baughman, R. H.; Kim, S. J. Flexible, Stretchable and Weavable Piezoelectric Fiber. *Adv. Eng. Mater.* **2015**, *17* (9), 1270–1275. <https://doi.org/10.1002/adem.201500018>.
- (24) Yang, Y.; Sun, N.; Wen, Z.; Cheng, P.; Zheng, H.; Shao, H.; Xia, Y.; Chen, C.; Lan, H.; Xie, X.; Zhou, C.; Zhong, J.; Sun, X.; Lee, S.-T. Liquid-Metal-Based Super-Stretchable and Structure-Designable Triboelectric Nanogenerator for Wearable Electronics. *ACS Nano* **2018**, *12* (2), 2027–2034. <https://doi.org/10.1021/acsnano.8b00147>.
- (25) Wang, L.; Liu, W.; Yan, Z.; Wang, F.; Wang, X. Stretchable and Shape-Adaptable Triboelectric Nanogenerator Based on Biocompatible Liquid Electrolyte for Biomechanical Energy Harvesting and Wearable Human–Machine Interaction. *Adv. Funct. Mater.* **2021**, *31* (7), 2007221. <https://doi.org/10.1002/adfm.202007221>.